Clim Dyn (2016) 47:2955–2974
DOI 10.1007/s00382-016-3007-9

Mechanisms for stronger warming over drier ecoregions observed since 1979

Liming Zhou[1] · Haishan Chen[2] · Wenjian Hua[3] · Yongjiu Dai[4] · Nan Wei[1,4]

Received: 11 June 2015 / Accepted: 21 January 2016 / Published online: 3 February 2016

Abstract Previous research found that the warming rate observed for the period 1979–2012 increases dramatically with decreasing vegetation greenness over land between 50°S and 50°N, with the strongest warming rate seen over the driest regions such as the Sahara desert and the Arabian Peninsula, suggesting warming amplification over deserts. To further this finding, this paper explores possible mechanisms for this amplification by analyzing observations, reanalysis data and historical simulations of global coupled atmosphere–ocean general circulation models. We examine various variables, related to surface radiative forcing, land surface properties, and surface energy and radiation budget, that control the warming patterns in terms of large-scale ecoregions. Our results indicate that desert amplification is likely attributable primarily to enhanced longwave radiative forcing associated with a stronger water vapor feedback over drier ecoregions in response to the positive global-scale greenhouse gas forcing. This warming amplification and associated downward longwave radiation at the surface are reproduced by historical simulations with anthropogenic and natural forcings, but are absent if only natural forcings are considered, pointing to new potential fingerprints of anthropogenic warming. These results suggest a fundamental pattern of global warming over land that depend on the dryness of ecosystems in mid- and low- latitudes, likely reflecting primarily the first order large-scale thermodynamic component of global warming linked to changes in the water and energy cycles over different ecosystems. This finding may have important implications in interpreting global warming patterns and assessing climate change impacts.

Keywords Global warming · Greenhouse gases · Radiative forcing · Water vapor feedback

✉ Liming Zhou
lzhou@albany.edu

[1] Department of Atmospheric and Environmental Sciences, University at Albany, State University of New York (SUNY), 1400 Washington Avenue, Albany, NY 12222, USA

[2] Collaborative Innovation Center on Forecast and Evaluation of Meteorological Disasters/Key Laboratory of Meteorological Disaster, Ministry of Education, Nanjing University of Information Science and Technology, Nanjing 210044, China

[3] College of Atmospheric Sciences, Nanjing University of Information Science and Technology, Nanjing 210044, China

[4] College of Global Change and Earth System Science, Beijing Normal University, Beijing 100875, China

1 Introduction

Globally averaged near surface temperatures have increased since the beginning of the 20th century, with the largest increase over land since the 1970s (IPCC 2013). This warming is not spatially uniform, and in particular, is much greater over land than oceans due to the ocean's larger heat capacity and higher evaporative cooling (e.g., Sutton et al. 2007), over the Northern Hemisphere than the Southern Hemisphere mainly because of meridional ocean heat transport (e.g., Wunsch 2005), over higher latitudes because of positive snow/ice-albedo feedbacks (e.g., Deser et al. 2000; Qu and Hall 2007) and strengthening of atmospheric circulation (e.g., Lu and Cai 2010), and over higher elevations associated with stronger water vapor and lapse-rate feedbacks (e.g., Rangwala et al. 2013; Naud et al. 2013).

In low- and mid-latitudes, the warming rate differs substantially among ecosystems. Zhou et al. (2015) analyzed the relationship between surface temperature trends

observed over land between 50°S and 50°N for the period 1979–2012 and enhanced vegetation index (EVI), a satellite measured vegetation greenness index, by large-scale ecoregion. They found that the warming rate increases dramatically with decreasing EVI, with the strongest warming rate seen over the least vegetated (or driest) regions such as the Sahara desert and the Arabian Peninsula, indicating warming amplification over deserts. This desert amplification is reproduced by historical simulations of global coupled atmosphere–ocean general circulation models (AOGCMs) when anthropogenic and natural forcings are included, but is absent if only natural forcings are considered. These results suggest a fundamental pattern of global warming over land that depend on the dryness of ecosystems in mid- and low-latitudes, pointing mainly to new potential fingerprints of anthropogenic warming.

Table 1 List of the datasets used in this study

Data provider	Data version	Variable	Spatial resolution	Period	References
CRU	TS3.22	P,T, TCC, DLR	0.5° × 0.5°	1979–2012	Harris and Jones (2014), Wang and Liang (2009)
ECMWF	ERA-Interim	DLR, DSR, *q*, P, T, TCC, T_d	0.5° × 0.5°	1979–2012	Harris and Jones (2014), ECMWF (2013)
HadCRU	HadCRUH	*q*	0.05° × 0.05°	1973–2003	Willett et al. (2008)
NASA	MOD13C2/C5	EVI	0.05° × 0.05°	2000–2012	Huete et al. (2002)
GISS	GISTEMP	T	2.5° × 2.5°	1979–2012	Hansen et al. (2010)
NCDC	MLOST/v3.5.3	T	5° × 5°	1979–2012	Vose et al. (2012)

Note that DLR in CRU is estimated from the CRU data of surface temperature, vapor pressure, cloud cover, and surface elevation following the methods of Wang and Liang (2009); near surface *q* in ERA is estimated from the ERA T_d and surface pressure following the methods of ECMWF (2013); other surface fluxes (downward shortwave radiation, net longwave radiation, net solar radiation, upward longwave radiation, reflected solar radiation, latent heat and sensible heat) in ERA are also used but not listed here

CRU Climatic Research Unit, *ECMWF* European Centre for Medium-Range Weather Forecasts, *GISS* Goddard Institute for Space Studies, *HadCRU* Hadley Centre and Climate Research Unit, *NASA* National Aeronautics and Space Administration, *NCDC* National Climatic Data Center, *HadCRUH* Hadley Centre and Climate Research Unit global surface humidity dataset, *TS* time-series, *MLOST* Merged Land–Ocean Surface Temperature Analysis, *DLR* downward longwave radiation at the surface (W/m^2), *DSR* downward shortwave radiation at the surface (W/m^2), *EVI* enhanced vegetation index, *P* precipitation (mm/day), *T* surface air temperature (°C), *TCC* total cloud cover (%), T_d surface dew point temperature (°C), *q* specific humidity (g/kg)

Table 2 List of 18 CMIP5 models with simulations used in ALL, RCP45, and NAT for the period 1979–2012

Organizations	Model[a]	ALL	RCP45	NAT
BCC/China Meteorological Administration, China	BCC-CSM1	*	*	*
Canadian Centre for Climate Modelling and Analysis, Canada	CanESM2	*	*	*
National Center for Atmospheric Research, USA	CCSM4	*	*	*
National Center for Atmospheric Research, USA	CESM1-CAM5	*	*	*
Centro Euro-Mediterraneo per I Cambiamenti Climatici, Italy	CMCC-CMS	*	*	
Centre National de Recherches Meteorologiques, France	CNRM-CM5	*	*	*
CSIRO Atmospheric Research, Australia	CSIRO-Mk3-6-0	*	*	*
Institute of Atmospheric Physics, China	FGOALS-g2	*	*	*
NOAA/Geophysical Fluid Dynamics Laboratory, USA	GFDL-CM3	*	*	*
NASA/Goddard Institute for Space Studies, USA	GISS-E2-R	*	*	*
Met Office Hadley Centre, UK	HadGEM2-ES	*	*	*
Institut Pierre-Simon Laplace, France	IPSL-CM5A-LR	*	*	*
JAMSTEC/AORI/NIES, Japan	MIROC-ESM	*	*	*
JAMSTEC/AORI/NIES, Japan	MIROC-ESM-CHEM	*	*	*
Max Planck Institute for Meteorology, Germany	MPI-ESM-LR	*	*	
Max Planck Institute for Meteorology, Germany	MPI-ESM-MR	*	*	
Norwegian Climate Center, Norway	NorESM1-ME	*	*	
Norwegian Climate Center, Norway	NorESM1-M	*	*	*

Note that simulations with both anthropogenic and natural forcings are referred to as ALL, and simulations with natural forcings only are referred to as NAT. Models with symbol "*" indicate that their simulations are available. Only one ensemble member "r1i1p1" from each model is used

[a] Each model is detailed at http://www-pcmdi.llnl.gov/ipcc/model_documentation/ipcc_model_documentation.php

Table 3 Seasonal variations in the fitted coefficients and goodness of fit (R^2) for the logarithmic and linear functions between observed T_{trend} (°C/10 years) and the climatological EVI by large-scale ecoregion

Ecoregions	$y = A_0 * EVI + C_0$		$y = A_0 * \ln(EVI) + C_0$	
	A_0	R^2	A_0	R^2
DJF (December–January–February)				
7	−0.11	0.08	0.00	0.00
14	−0.09	0.03	0.01	0.01
21	−0.08	0.02	0.01	0.02
28	−0.08	0.02	0.02	0.03
35	−0.08	0.02	0.02	0.04
MAM (March–April–May)				
7	−0.76	0.96	−0.16	0.95
14	−0.77	0.94	−0.16	0.94
21	−0.77	0.92	−0.16	0.93
28	−0.77	0.92	−0.16	0.93
35	−0.77	0.90	−0.16	0.91
JJA (June–July–August)				
7	−0.33	0.85	−0.08	0.97
14	−0.33	0.76	−0.08	0.90
21	−0.33	0.67	−0.08	0.80
28	−0.33	0.67	−0.08	0.80
35	−0.33	0.63	−0.08	0.75
SON (September–October–November)				
7	−0.35	0.87	−0.08	0.92
14	−0.34	0.76	−0.08	0.82
21	−0.34	0.75	−0.07	0.81
28	−0.34	0.71	−0.07	0.78
35	−0.34	0.71	−0.07	0.77
ANN (annual mean)				
7	−0.42	0.92	−0.09	0.96
14	−0.42	0.88	−0.09	0.93
21	−0.42	0.88	−0.09	0.93
28	−0.42	0.86	−0.09	0.90
35	−0.41	0.85	−0.09	0.89

The magnitude of warming depends on surface radiative forcing and terrestrial responses and feedbacks (Hansen et al. 2010; Thorne et al. 2010). Evapotranspiration (ET) is a primary process driving energy and water exchanges between the hydrosphere, atmosphere and biosphere (Wang and Dickinson 2012) and thus may determine surface warming rates among different ecosystems. EVI largely reflects the geographical distribution of amount of vegetation and soil moisture (SM; Zhou et al. 2015) and thus correlates highly with ET, particularly at large scales (Suzuki and Masuda 2004; Nagler et al. 2005). It is expected that radiative forcing at land surface would be largely weakened by ET over regions with increasing EVI (Jeong et al. 2009; Zhou et al. 2007, 2009, 2010). However, this mechanism should work primarily in regions where SM and vegetation are the main controlling factors for ET (Seneviratne et al. 2010). The driest ecoregions such as the Sahara desert and the Arabian Peninsula have very limited amounts of vegetation and SM, very high surface albedo and little cloud cover. Small decadal variations in solar irradiance will not have significant impacts on surface warming. Large changes in land surface properties (e.g., albedo, emissivity, roughness) and land cover/use are unlikely over these regions. Hence new mechanisms are needed to explain the strongest warming trends observed over the driest ecosystems.

This study focuses on understanding and attributing spatiotemporal patterns of temperature trends observed for the period 1979–2012, with an emphasis on exploring possible relevant physical mechanisms, by analyzing observations, reanalysis data and historical simulations of AOGCMs developed for the Coupled Model Intercomparison Project phase 5 (CMIP5) (Taylor et al. 2012). We hypothesize that desert amplification may be attributable primarily to enhanced longwave radiative forcing associated with a stronger water vapor feedback over drier ecosystems in response to the positive global-scale greenhouse gas (GHG) forcing.

2 Data and methods

For observations (referred to as OBS), three widely-used surface air temperature (T) datasets: CRU (Harris and Jones 2014), GISS (Hansen et al. 2010) and NCDC (Vose et al. 2012), for the period 1979–2012 are considered. The three datasets show very similar T changes and so their ensemble mean is used to reduce redundancy as done in Zhou et al. (2015). In addition, MODIS EVI (Huete et al. 2002) for the period 2000–2012, HadCRUH surface specific humidity (Willett et al. 2008) for the period 1973–2003, and the ERA-interim reanalysis data (Dee et al. 2011, referred to as ERA) for the period 1979–2012 are also examined. More specifics of each dataset are listed in Table 1.

For historical simulations, we use monthly output of 18 participant AOGCMs (Table 2), which have 6 more models compared to Zhou et al. (2015). These simulations include time-evolving changes in anthropogenic (greenhouse gases and sulfate aerosols) and/or natural (solar and volcanic) forcing agents for the period 1860–2005, extended for the years 2006–2012 with the RCP4.5 scenario runs. They are divided into two groups: one with anthropogenic and natural forcings (referred to as ALL) and the other with only natural forcings (referred to as NAT). As averaging over multiple members enhances the forcing signal and reduces noise from internal variability and errors from individual models (IPCC 2013), we simply average the available simulations to obtain the multi-model ensemble mean in ALL for the period 1979–2012 and in NAT for the period 1979–2005. However, the ensemble mean tends to average out internal variability

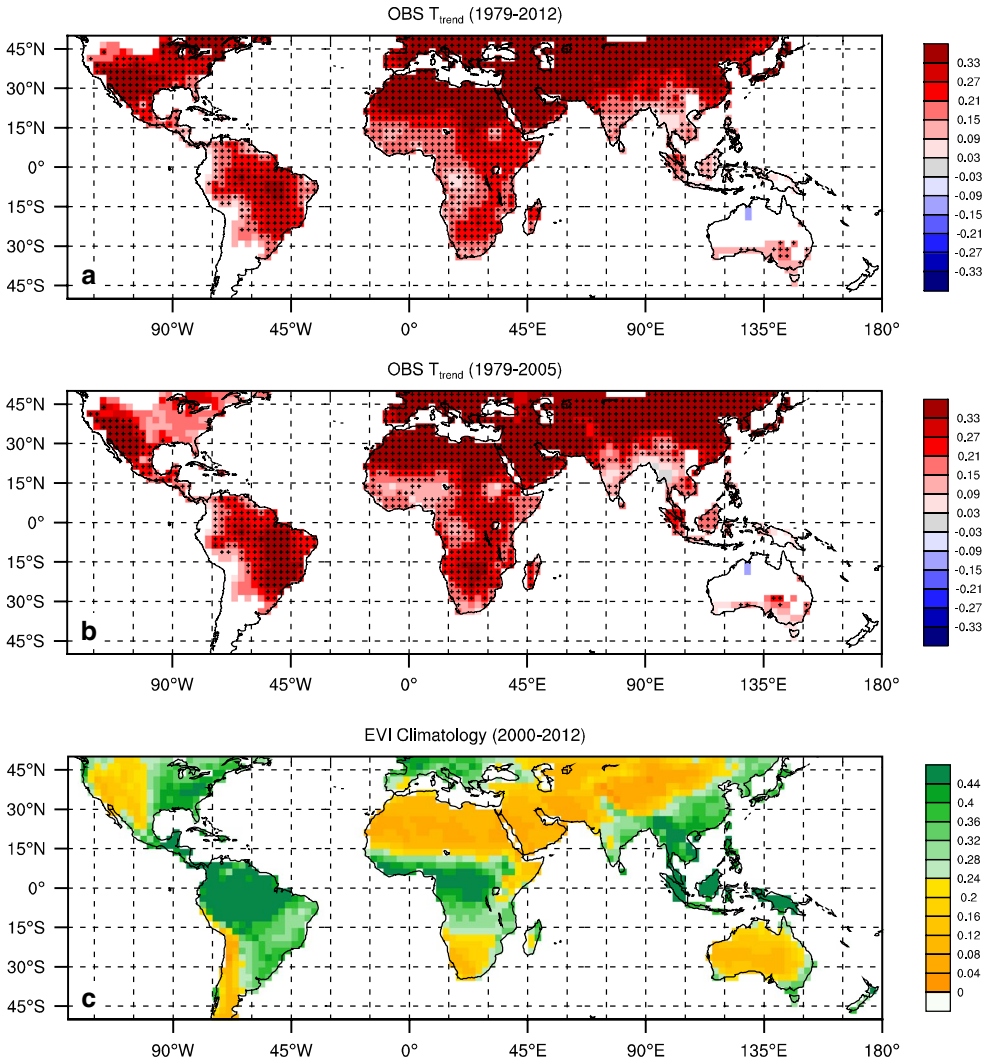

Fig. 1 Spatial patterns of T_{trend} (°C/10 years) in the months of March–November (M–N) for the period **a** 1979–2012 and **b** 1979–2005. *Stippling* indicates regions where T_{trend} is statistically significant ($p < 0.05$). The ensemble mean of three observational temperature datasets (CRU, GISS and NCDC) is used to calculate the mean T_{trend} (Zhou et al. 2015). **c** Spatial patterns of climatological EVI in M–N for the period 2000–2012

as each individual simulation was initialized from a different point of control runs. Hence we also analyze the 14 individual simulations in NAT because internal variations may play a role in forming the spatial patterns of warming as well.

For the ERA and CMIP5 data, we examine monthly means of precipitation, total cloud cover (TCC), specific humidity (q), radiative fluxes at the surface (downward longwave radiation (DLR), downward shortwave radiation (DSR), net longwave radiation, net solar radiation, upward longwave radiation, and reflected solar radiation), and surface non-radiative fluxes (latent heat and sensible heat). All variables are spatially re-projected into 2.5° × 2.5° grid boxes. The monthly EVI is aggregated to create the climatology of seasonal and annual mean EVI. The monthly data of other variables are temporally averaged to generate seasonal and annual mean (ANN) anomalies. Seasons are defined as follows: December–January–February (DJF), March–April–May (MAM), June–July–August (JJA), September–October–November (SON), and March–November (M–N).

We focus only on 1338 land grid boxes in the low- and mid-latitudes (50°N–50°S) that have adequate observations and show a statistically significant ($p < 0.1$) T_{trend} in ANN during the period 1979–2012 following the selection criteria of Vose et al. (2012) and Zhou et al. (2015). The land beyond 50°N and 50°S is excluded to minimize polar warming amplification and snow/ice-albedo feedbacks that dominate the high-latitude warming. ERA data and CMIP5 simulations are sampled so that coverage corresponds to that of the observations considered. For a time series at a given grid box, a linear trend is estimated using least squares fitting and a two-tailed Student's t test is used to quantify whether the trend differs significantly from zero. For simplicity, we refer to the trends of four most used variables, T, DLR, TCC and q, as T_{trend}, DLR_{trend}, TCC_{trend} and q_{trend}, respectively.

As our emphasis is large-scale T_{trend} and its attribution, we analyze primarily the results of ANN or M–N at large ecoregions because other factors such as sea surface temperature (SST) may play an increasing role in influencing seasonal

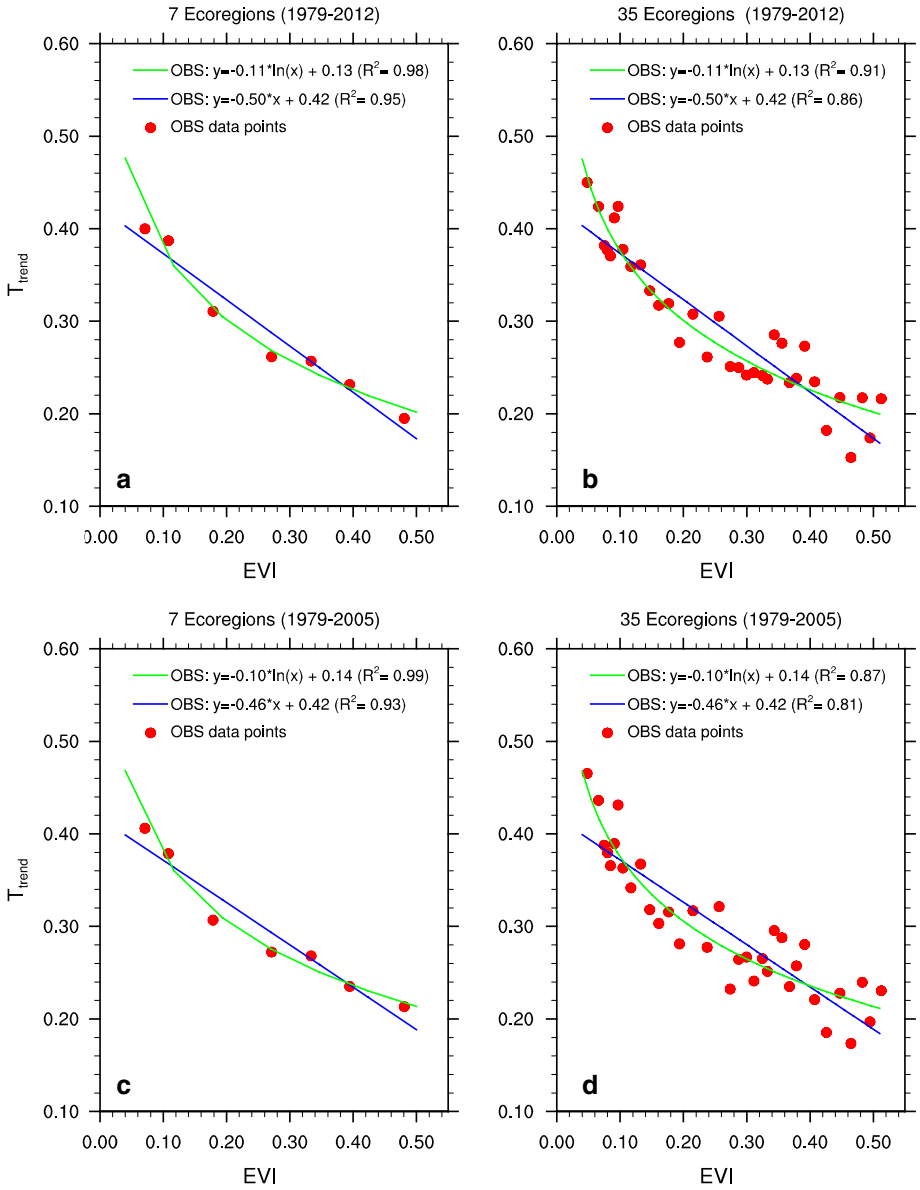

Fig. 2 **a**, **b** Relationship between observed T_{trend} (°C/10 years) for the period 1979–2012 and the climatological EVI by large-scale ecoregion in the months of March–November (M–N). Least squares fittings of linear and logarithmic functions, with the fitted coefficients and goodness of fit (R^2), are shown. **c**, **d** Same as (**a**, **b**) but for the period 1979–2005

T_{trend} (Zhou et al. 2015) and climate models have difficulties in simulating small-scale processes (IPCC 2013). We classify the 1338 grids into 7, 14, 21, 28, and 35 large-scale ecoregions from barren to dense vegetation based on the climatological EVI values, and then analyze how T_{trend} varies with EVI by ecoregion via least squares fitting. The goodness of fit (R^2) is used to measure how well the fit is in capturing the data variance. Different classifications are used to test whether the fitted T_{trend}–EVI relationship is robust. For each classification, every ecoregion contains about the same number of grid boxes. The areal mean time series is calculated using area-weighted averaging over the land grids within each ecoregion, and its trend is estimated as done at the grid level. For brevity, only results of 7 and 35 ecoregions, which represent the least and most ecoregions classified, are shown in figures, while results of other classifications are listed in tables.

3 Results and discussion

3.1 Temperature trends in observations

Zhou et al. (2015) analyzed the observed T_{trend} and its spatial dependence on the climatology of EVI using the annual mean data. At the grid level, strong and significant warming trends were mostly seen over very dry regions. At the large-scale ecoregion level, five different regression lines (exponential, linear, logarithmic, polynomial and power) were fit for the areal mean T_{trend} and EVI. All fits shows consistently stronger warming rates over drier ecosystems, with the best fit for the negative logarithmic function and the least fit for the linear function.

Table 4 The fitted coefficients and goodness of fit (R^2) for the linear and logarithmic functions between observed T_{trend} (°C/10 years) and DLR_{trend} (W/m^2/10 years) and the climatological EVI by large-scale ecoregion during the months of March–November (M–N)

Ecoregions	$y = A_0 * EVI + C_0$		$y = A_0 * \ln(EVI) + C_0$	
	A_0	R^2	A_0	R^2
Observed T_{trend}				
7	−0.50	0.95	−0.11	0.98
14	−0.50	0.92	−0.11	0.96
21	−0.50	0.88	−0.11	0.93
28	−0.50	0.90	−0.11	0.94
35	−0.50	0.86	−0.11	0.91
Estimated DLR_{trend} from CRU				
7	−4.42	0.75	−1.04	0.91
14	−4.45	0.69	−1.06	0.87
21	−4.41	0.66	−1.05	0.84
28	−4.43	0.64	−1.06	0.82
35	−4.42	0.62	−1.06	0.79
ERA T_{trend}				
7	−0.43	0.82	−0.09	0.85
14	−0.43	0.76	−0.10	0.81
21	−0.43	0.71	−0.09	0.78
28	−0.43	0.67	−0.10	0.73
35	−0.43	0.63	−0.09	0.68
ERA DLR_{trend}				
7	−1.98	0.81	−0.46	0.95
14	−1.98	0.74	−0.46	0.90
21	−1.97	0.68	−0.46	0.83
28	−1.98	0.66	−0.47	0.82
35	−1.97	0.65	−0.46	0.79

Note that DLR_{trend} in CRU is estimated from the CRU data (see Table 1 for detail)

We perform similar analyses to examine whether the T_{trend}–EVI relationship obtained from ANN in Zhou et al. (2015) varies with seasons (Table 3). This study focuses mostly on the negative logarithmic T_{trend}–EVI fit because it generally has the highest R^2 among the five fitting functions, while the linear fit is also included for comparison purpose. The results are consistent across all classifications and all seasons except for DJF when there is no spatial dependence of T_{trend} on EVI. For MAM, JJA, SON and ANN, the negative logarithmic fit always works better than the linear fit, with the R^2 values comparable to the ANN results. The fitted coefficient (A_0) decreases slightly with the increasing number of ecoregions, and so does R^2. When more ecoregions (or EVI bins) are considered, R^2 decreases as more small-scale factors affect the spatial variations of T_{trend}. We also perform the same fitting for the period 1979–2005 as the NAT simulations end in 2005, and obtain similar results. Given the absence of a meaningful T_{trend}–EVI relationship in DJF, we focus the remaining analysis on the 9-month period of M–N.

Figure 1a shows the spatial patterns of observed M–N T_{trend} over the study region for the period 1979–2012, together with the climatology of M–N EVI (Fig. 1c). T increases almost everywhere and significant warming occurs mostly in arid and semi-arid regions such as Northern Africa, Middle East, Northern China, and western US. Among the 1338 grids, 95 % show a statistically significant T_{trend} ($p < 0.05$). The warming trend is generally strongest over the driest or least vegetated regions such as the Sahara desert and the Arabian Peninsula. Such warming patterns remain similar for the period 1979–2005 (Fig. 1b). Note that comparable warming trends are also observed over few non-dry regions such as the continental Europe and the eastern and southern Amazonian regions. The European warming is consistent with surface observations where the significant warming rate after 1988 is attributed to increases in q and DLR, not to radiative effects due to changes in solar radiation and clouds (Philipona et al. 2005). The eastern and southern Amazonian warming may be associated with anomalies in sea surface temperature in both the Atlantic and Pacific regions (Malhi and Wright 2004; Jiménez-Muñoz et al. 2013). Nevertheless, the spatial correlation between T_{trend} and EVI is −0.53 for the period 1979–2012 and −0.47 for the period 1979–2005, all statistically significant ($p < 0.001$, n = 1338).

Figure 2 shows the observed M–N T_{trend} as a function of M–N EVI in terms of 7 and 35 ecoregions. Evidently, the warming rate depends strongly on ecoregions. T_{trend} increases dramatically with decreasing EVI, indicating the lower the vegetation greenness, the stronger the warming trend. The negative logarithmic fit is better than the linear fit, with R^2 = 98 and 91 % (R^2 = 95 and 86 %) for the former (the latter) for the classification of 7 and 35 ecoregions, respectively. Other classifications (Table 4) agree that the negative logarithmic fit better describes the T_{trend}–EVI relationship than the linear fit by ecoregion. Furthermore, the results for the period 1979–2005 (Fig. 2c, d) are very similar to those for the period 1979–2012 (Fig. 2a, b).

3.2 Temperature trends in ERA and CMIP5

It is essential that the ERA reanalysis and CMIP5 simulations can reproduce the major T_{trend} features in OBS before being used for attribution. Figure 3a illustrates the areal mean M–N T anomalies for OBS, ERA and ALL from 1979 to 2012 averaged over the entire study region (i.e., the 1338 land grids). ERA resembles OBS not only in the interannual variability but also in the linear trend (0.29 ± 0.03 °C/10 years, $p < 0.001$). ALL reproduces the majority of T variability and slightly overestimates the warming trend (0.35 ± 0.03 °C/10 years, $p < 0.001$). Figure 3b–e display the areal mean M–N T anomalies for the driest and wettest climate in terms of 7 and 35 ecoregions.

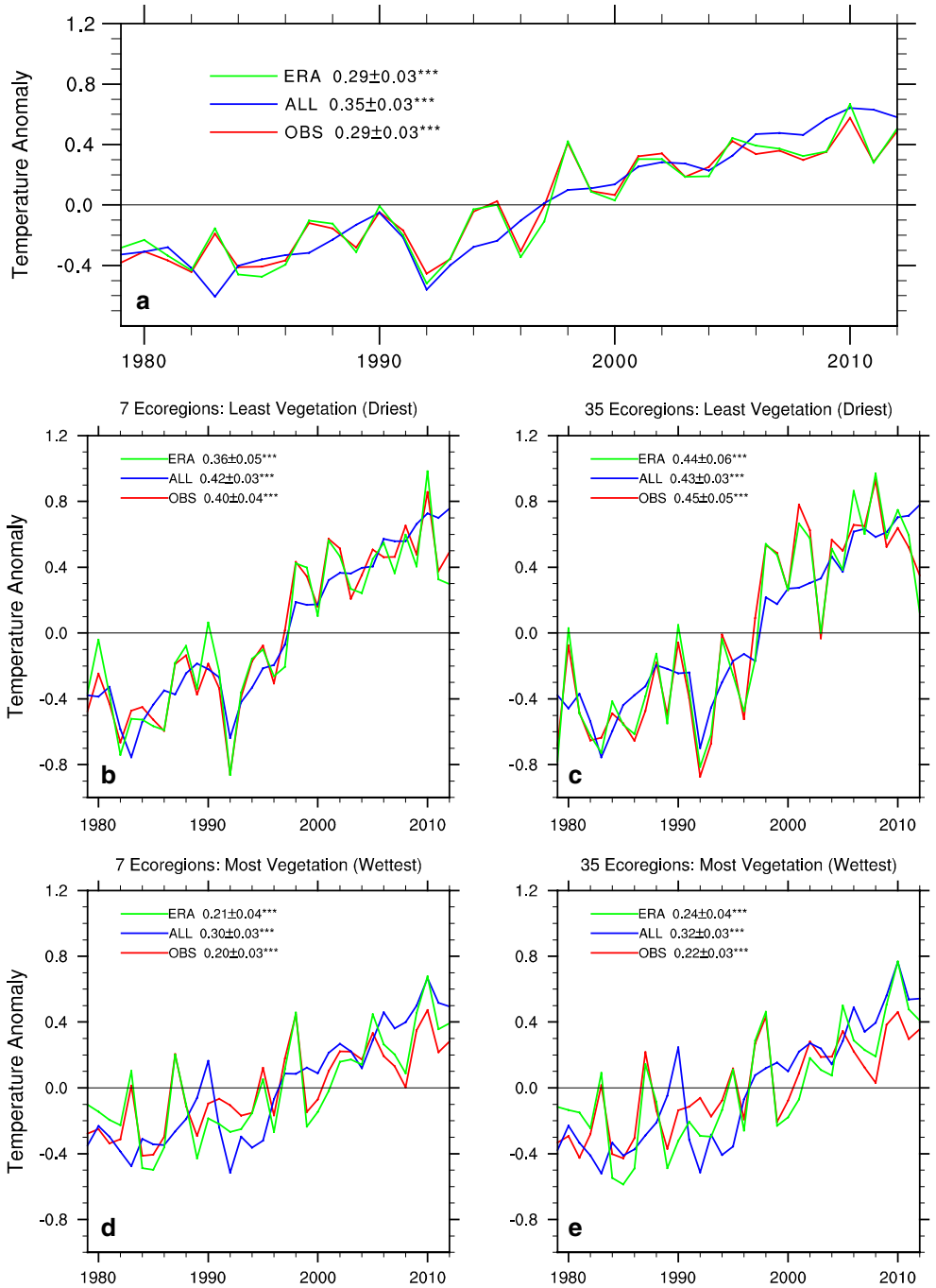

Fig. 3 Areal mean temperature anomalies from OBS, ERA and ALL in the months of March–November (M–N) for the period 1979–2012 averaged over **a** the 1338 land grids between 50°S and 50°N, **b** the driest ecoregion in terms of 7 large-scale ecoregions, **c** the driest ecoregion in terms of 35 large-scale ecoregions, **d** the wettest ecoregion in terms of 7 large-scale ecoregions, and **e** the wettest ecoregion in terms of 35 large-scale ecoregions. Linear trends (°C/10 years) plus one standard deviation with "***" are statistically significant ($p < 0.001$)

In every ecoregion, the three T datasets exhibit similar interannual variability and comparable warming trends that are all statistically significant ($p < 0.001$), with stronger warming rates over drier ecosystems. ERA and ALL generally reproduce the observed warming trends very well at every ecoregion, with a warming rate differing slightly from OBS. ERA captures interannual T variability and the warming magnitude better than ALL, which is expected as the multi-model ensemble mean in ALL represents primarily the forced signal (Dai 2013). ALL slightly overestimates the

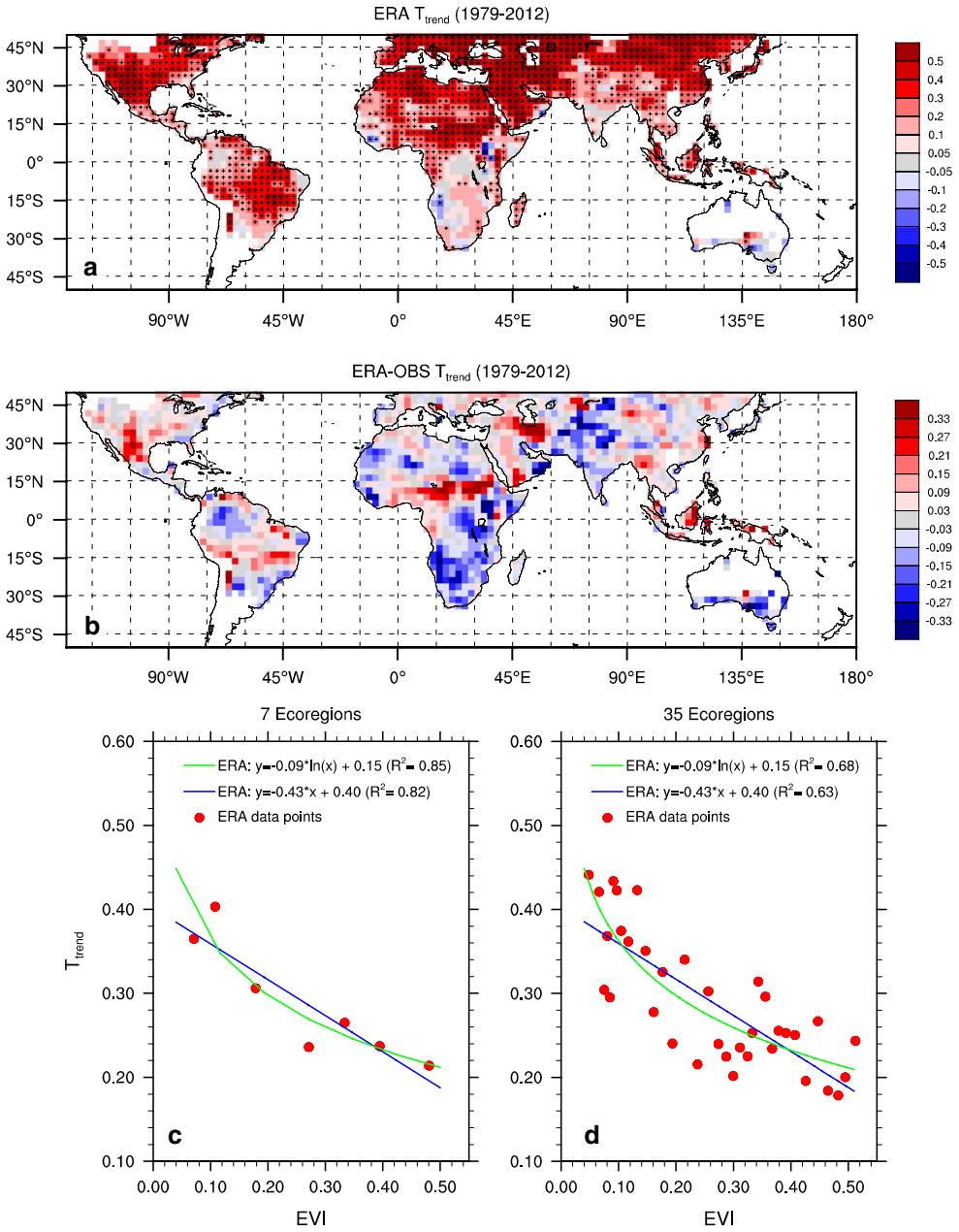

Fig. 4 Spatial patterns of **a** ERA T_{trend} (°C/10 years) and **b** its biases from observations (ERA − OBS) in the months of March–November (M–N) for the period 1979–2012. *Stippling* indicates regions where T_{trend} is statistically significant ($p < 0.05$). **c**, **d** Same as Fig. 2a, b but for the ERA T_{trend} (°C/10 years)

warming trend because the simulated T anomalies are higher than OBS during the global warming hiatus (IPCC 2013).

Figure 4a shows the spatial patterns of ERA T_{trend} in M–N over land for the period 1979–2012. The warming is widespread and shows spatial patterns similar to OBS (Fig. 1a). Among the 1338 land grids, 77 % exhibit a statistically significant linear trend ($p < 0.05$), which is much lower than OBS. The spatial correlation between ERA T_{trend} and EVI is −0.30 ($p < 0.001$, n = 1338), which is lower than OBS as well. At the ecoregion level, the observed T_{trend}–EVI relationship holds true also in ERA and the logarithmic fit performs always better than the linear fit (Fig. 4c, d). The R^2 value for the logarithmic fit is 85 and 68 % for the 7 and 35 ecoregions, respectively. The corresponding values for the linear fit are 82 and 63 %. Other classifications (Table 4) agree consistently that the negative logarithmic fit best describes the T_{trend}–EVI relationship by ecoregion in ERA.

Figure 5a shows the spatial patterns of ALL T_{trend} in M–N over land for the period 1979–2012. The warming is

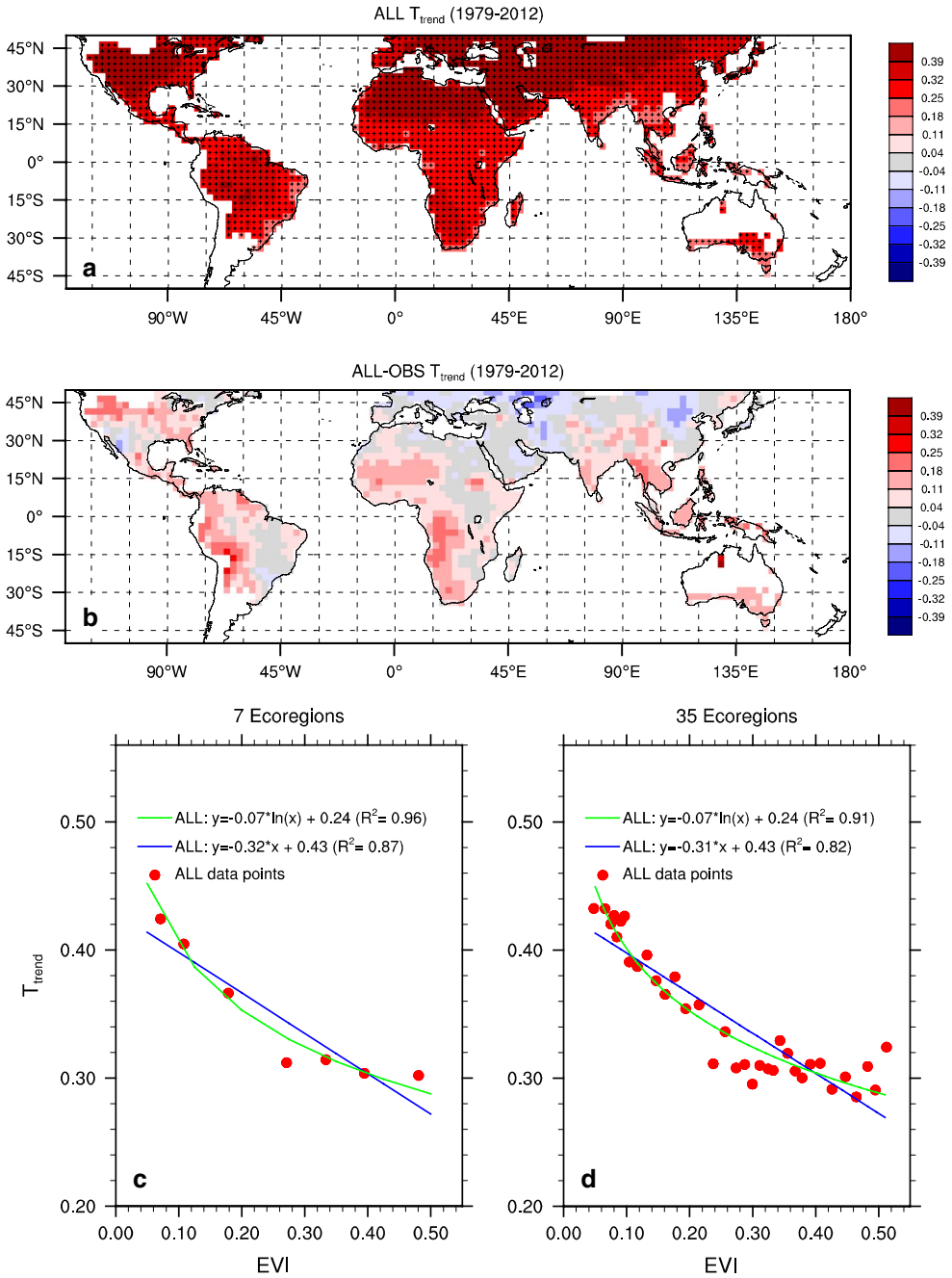

Fig. 5 Same as Fig. 4 but for the CMIP5 multi-model ensemble mean T_{trend} (°C/10 years) in ALL

ubiquitous and the strongest warming occurs primarily in arid and semi-arid regions such as Northern Africa, Middle East, and western US. Among the 1338 land grids, 100 % exhibit a statistically significant linear trend ($p < 0.05$), which is much higher than OBS. The spatial correlation between ALL T_{trend} and EVI is −0.57 ($p < 0.001$, n = 1338), which is higher than OBS as well. ALL slightly underestimates the warming magnitude in Eurasia and overestimates the warming rate elsewhere (Fig. 5b), possibly due to models' difficulties in simulating T changes at small scales (IPCC 2013). At the ecoregion level, the observed T_{trend}–EVI relationship remains true also in ALL. The R^2 value for the logarithmic (linear) fit is 96 and 91 % (87 and 82 %) for the 7 and 35 ecoregions, respectively. Other classifications (Table 5) support consistently that the negative logarithmic fit better describes the T_{trend}–EVI relationship in ALL by ecoregion than the linear fit.

Figure 6a–c display the spatial patterns of T_{trend} and the T_{trend}–EVI relationship by ecoregion in the ensemble mean in NAT. The warming trend is strongest in several transitional climate zones at the grid level (more discussion in Sect. 3.3.2). At the ecoregion level, T_{trend} shows the largest

Table 5 Same as Table 4 but for the multi-model ensemble mean T_{trend} (°C/10 years) and DLR_{trend} (W/m^2/10 years) in ALL and NAT

Ecoregions	$y = A_0 * EVI + C_0$		$y = A_0 * \ln(EVI) + C_0$	
	A_0	R^2	A_0	R^2
ALL T_{trend}				
7	−0.32	0.87	−0.07	0.96
14	−0.31	0.85	−0.07	0.95
21	−0.31	0.84	−0.07	0.94
28	−0.31	0.83	−0.07	0.93
35	−0.31	0.82	−0.07	0.91
ALL DLR_{trend}				
7	−1.72	0.68	−0.42	0.87
14	−1.71	0.64	−0.41	0.82
21	−1.71	0.62	−0.41	0.80
28	−1.70	0.61	−0.41	0.78
35	−1.70	0.60	−0.40	0.77
NAT T_{trend}				
7	−0.07	0.60	−0.01	0.55
14	−0.07	0.56	−0.01	0.49
21	−0.07	0.53	−0.01	0.46
28	−0.07	0.50	−0.01	0.43
35	−0.07	0.47	−0.01	0.40
NAT DLR_{trend}				
7	0.06	0.10	0.01	0.12
14	0.06	0.08	0.01	0.08
21	0.06	0.05	0.01	0.06
28	0.06	0.05	0.01	0.06
35	0.06	0.04	0.01	0.05

warming rate over ecoregions with EVI between 0.1 and 0.2, not the driest ecoregions where the largest warming is observed. Evidently, the spatial patterns of T_{trend} and the T_{trend}–EVI relationship in NAT differ from those in OBS, ERA and ALL, and none of the 14 individual simulations in NAT exhibits the strongest warming trend over the driest ecoregions (Fig. 6d, e), pointing to anthropogenic causes of desert amplification.

Overall ERA and ALL largely reproduce the observed spatial patterns of T_{trend} at the grid level and the negative logarithmic T_{trend}–EVI relationship at the ecoregion level. The spatial correlation is 0.71 ($p < 0.001$, n = 1338) between OBS and ERA and is 0.82 ($p < 0.001$, n = 1338) between OBS and ALL. Compared to OBS, ERA T_{trend} is spatially less coherent while ALL T_{trend} is the opposite. Accordingly, at the ecoregion level, ALL has higher R^2 values than ERA, indicating that ALL can better capture the observed large-scale T_{trend}–EVI dependence. Note that the R^2 values for ERA and ALL are slightly smaller than OBS due to biases in both datasets (more discussion in Sect. 3.3.3). The negative logarithmic T_{trend}–EVI relationship indicates that the warming rate increases dramatically with decreasing EVI, suggesting warming amplification over very dry ecosystems.

3.3 Possible mechanisms

The warming rate of T_{trend} is determined by the magnitude of surface radiative forcing and any feedbacks involved related to land surface and atmospheric boundary layer (ABL) processes (Zhou et al. 2009, 2010; McNider et al. 2012; Dirmeyer et al. 2013; Davy and Esau 2014). Our results next support that the negative logarithmic T_{trend}–EVI relationship shown above may reflect primarily a stronger water vapor feedback over drier ecosystems under increasing GHGs.

3.3.1 Atmospheric water vapor feedback

Radiative forcing drives much of long-term climate change and global warming in the last three decades has been attributable to a predominance of GHG effects relative to aerosol effects (Hansen et al. 2010; Thorne et al. 2010; Foster and Rahmstorf 2011). The surface and lower troposphere are warmed primarily by GHGs-enhanced DLR as amplified by the associated increase of atmospheric water vapor content (AWV) observed since the 1980s (Held and Soden 2000; IPCC 2007; Dessler and Davis 2010). Figure 7 shows the grid-level scatter plots of DLR and the ratio of DLR_{trend} to AWV trend ($\partial DLR/\partial AWV$), which quantifies the sensitivity of DLR to changes in AWV as a function of climatological AWV in ALL for the period 1979–2012. The best fitted functions indicate that DLR is a power function of AWV ($DLR = 161.23 * AWV^{0.25}$, $R^2 = 0.90$, n = 1338) and $\partial DLR/\partial AWV$ decreases dramatically with increasing AWV following a negative logarithmic relationship ($\partial DLR/\partial AWV = -4.06 * \ln(AWV) + 17.63$, $R^2 = 0.88$, n = 1338). These results are consistent with previous studies from both observations and numerical models (e.g., Myhre et al. 1998; Ruckstuhl et al. 2007; Rangwala et al. 2013; Naud et al. 2013). Note that the spatial correlation of climatological values between AWV and EVI is 0.77 ($p < 0.001$, n = 1338), indicating that EVI can be used as a very good indicator of AWV at the grid level. Therefore, the negative logarithmic T_{trend}–EVI relationship might be attributable to enhanced DLR associated with a larger positive water vapor feedback over drier ecosystems. In other words, for a given amount of AWV increase, the largest efficiency in increasing DLR will occur over the driest regions where the AWV content is the least (Zhou et al. 2009, 2010). Validating this inference, however, remains challenging as long-term and consistent DLR and AWV observations at global scale are not available (Schneider et al. 2010). Next we examine

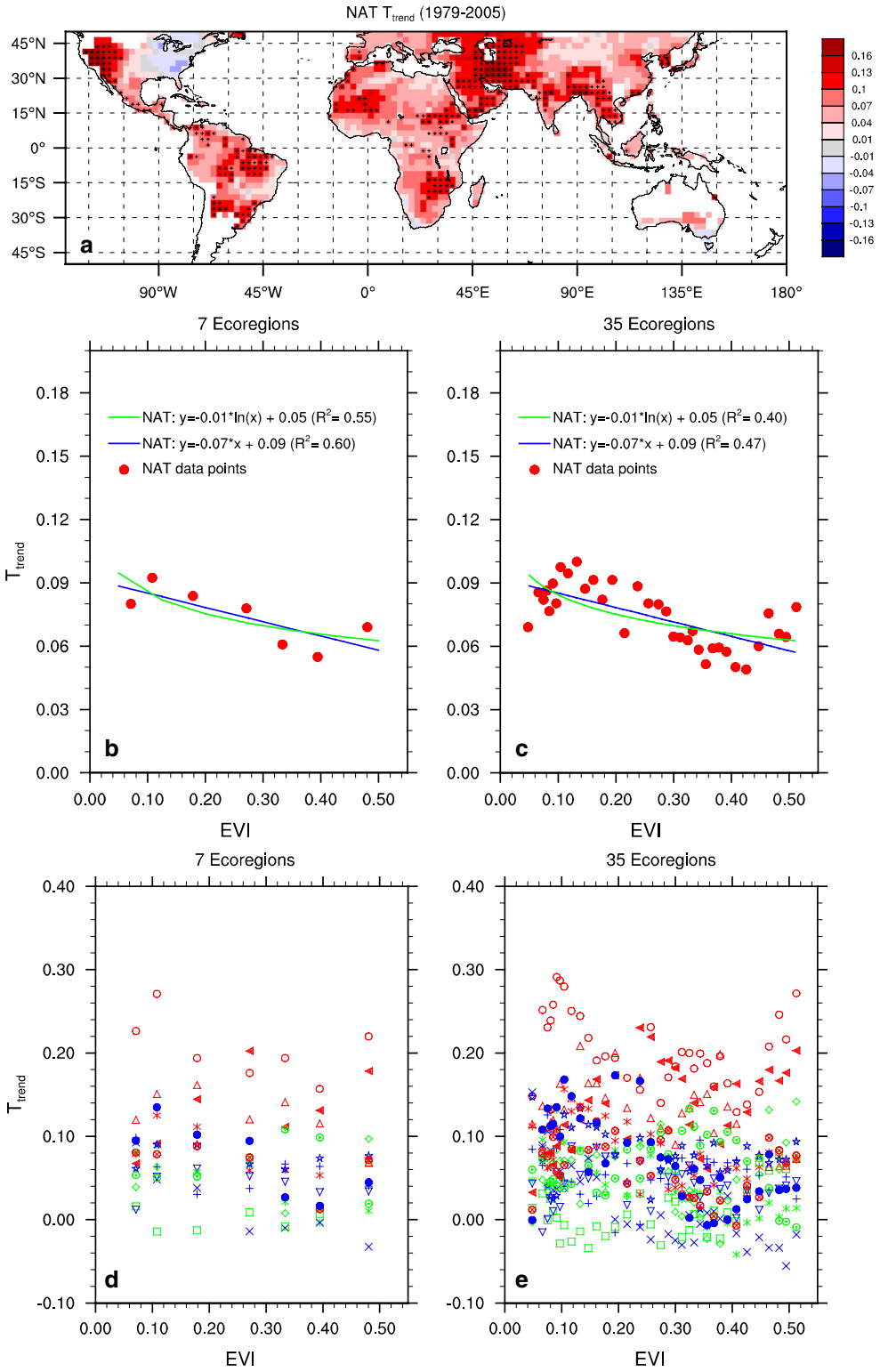

Fig. 6 **a–c** Same as Fig. 5a, c, d but for the CMIP5 multi-model ensemble mean T_{trend} (°C/10 years) in NAT. **d**, **e** Same as Fig. 6b, c but for the 14 individual simulations in NAT

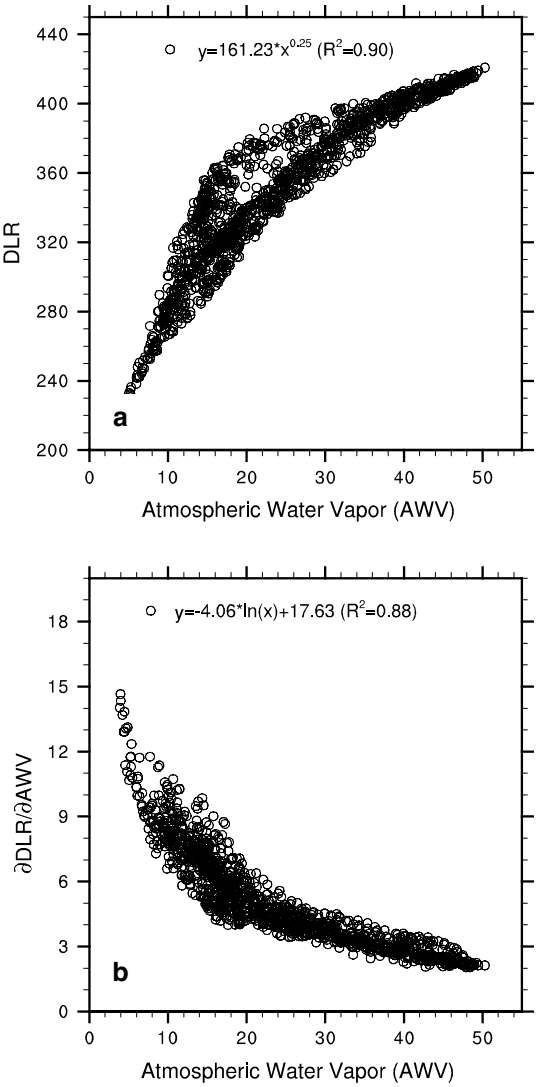

Fig. 7 Scatter plots of **a** DLR (W/m^2) and **b** the ratio of DLR_{trend} to AWV trend (∂DLR/∂AWV, W/kg) as a function of climatological atmospheric water vapor content (AWV, kg/m^2) at the grid level for the period 1979–2012 in ALL. The fitted coefficients and goodness of fit (R^2) for the best fitted function are listed

observations, reanalysis data and CMIP5 simulations to test this hypothesis.

We estimate surface q_{trend} from HadCRUH in M–N for the period 1973–2003. Despite many missing data over the study region, the observed q shows a widespread increasing trend in the NH, particularly over the regions such as Europe, west Central Africa and East Asian where the T increased most (Fig. 8a). Among the land grids without missing data, 72 % exhibit a statistically significant positive trend ($p < 0.05$) for q_{trend}. Analyses of near-global (60°S–75°N) synoptic data from >15,000 land stations found that surface q averaged over the global land increased by 4.3 % per 1 °C warming for the period 1976–2004 (Dai 2006). This increase in q is also consistent with surface observations in Europe where the significant warming after 1988 is attributed to increased q and DLR (Philipona et al. 2005).

Wang and Liang (2009) show that some empirical equations can provide very good estimates of DLR worldwide using surface observations from weather stations as most of AWV is confined near the surface. Following their approaches, we use the monthly CRU data to estimate DLR and its trend (DLR_{trend}). DLR_{trend} increases almost everywhere and the increase is generally strongest over driest regions (Fig. 8b). Among the 1338 land grids, 60 % exhibit a statistically significant positive trend ($p < 0.05$). At the ecoregion level, there is a negative logarithmic DLR_{trend}–EVI relationship (Fig. 8c, d), with $R^2 = 91$ and 79 % for the case of 7 and 35 ecoregions, respectively. The corresponding R^2 values for the linear fit are 75 and 62 %. Similar results are also seen for other classifications (Table 4). Note that the DLR_{trend}–EVI relationship has a smaller R^2 than the T_{trend}–EVI relationship, because DLR is roughly estimated using simple empirical equations with fixed parameters globally based on the CRU surface observations, which have large uncertainties over data-scarce regions such as Amazon and Central Africa (Harris and Jones 2014). Furthermore, DLR is also affected by changes in cloud cover and reanalysis data show large differences in DLR variability and trend (Wang and Dickinson 2013a).

Previous studies show that there is a strong positive connection between surface warming and increasing atmospheric q, and this connection is particularly strong in the tropical mid- and upper-troposphere such as 500 mb (Paltridge et al. 2009; Dessler and Davis 2010). Figure 9a, b show the spatial patterns of surface and 500 mb q_{trend} from ERA. Note that q has a unit of percentage change (%) relative to the climatological q as it is the fractional change in water vapor that matters in DLR_{trend} (Held and Soden 2000; Dessler et al. 2008). The 500 mb q increases almost everywhere in the tropics except parts of China, eastern Amazonia and western Central Africa (Fig. 9a). The positive q_{trend} in the driest regions such as the Sahara desert and the Arabian Peninsula is particularly important to the surface warming because the water vapor feedback is much stronger over drier ecosystems with lower q (e.g., Held and Soden 2000; Dessler and Davis 2010). The surface q also increases in many regions, particularly over the Sahara desert and the Arabian Peninsula, Asia, Europe and eastern North America (Fig. 9b). Note that surface q (not provided by ERA) is estimated based on 2 m dew point temperature and surface pressure and thus may have large uncertainties at regional and local scales. These results agree generally with Simmons et al. (2010), who compared surface q changes between HadCRUH and ERA for the period 1973–2008. Despite some issues with reanalysis in estimating

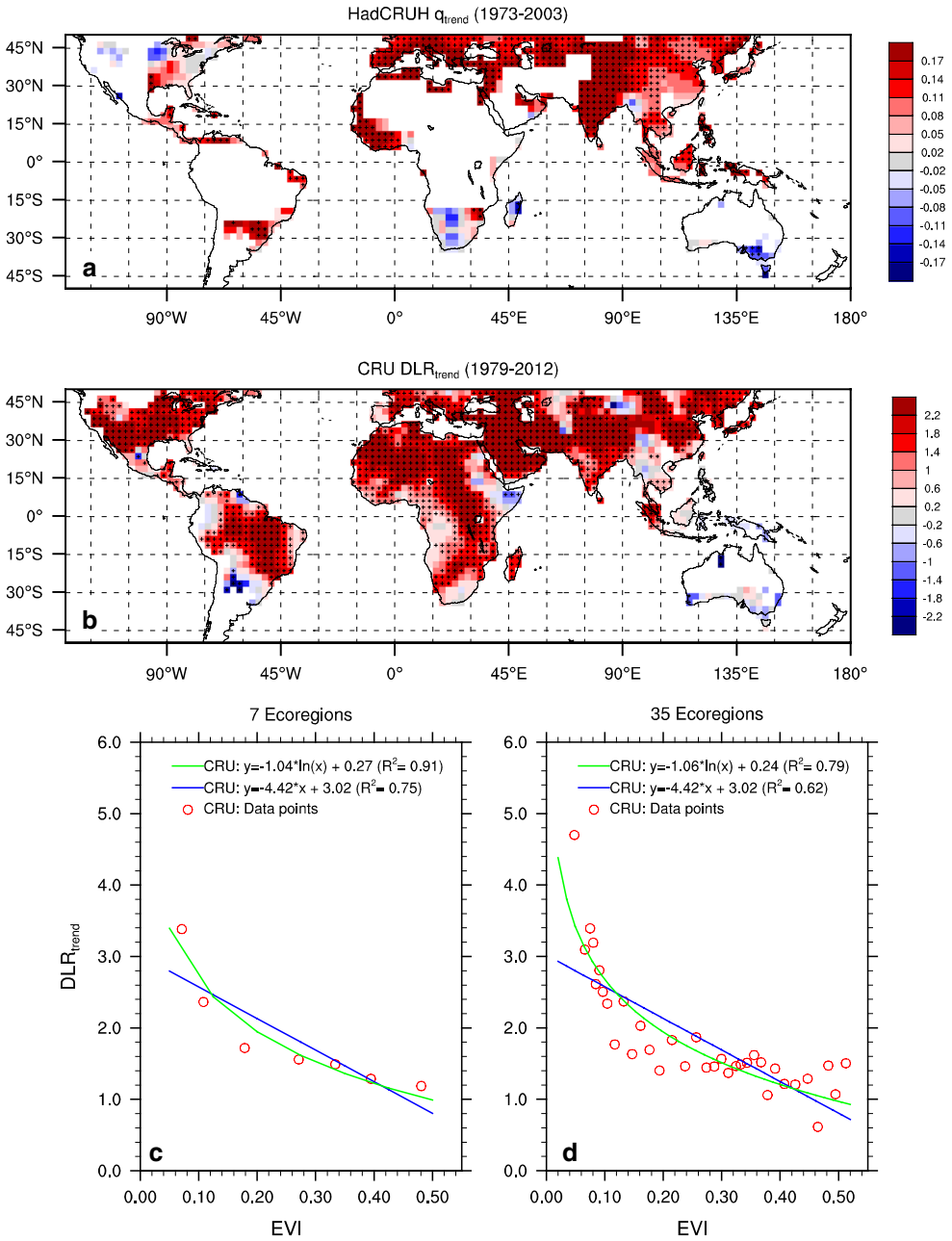

Fig. 8 Spatial patterns of **a** HadCRUH surface q_{trend} (g/kg/10 years) and **b** DLR_{trend} (W/m^2/10 years) in the months of March–November (M–N) for the period 1979–2012. *Stippling* indicates regions where the trend is statistically significant ($p < 0.05$). **c**, **d** Same as Fig. 2a, b but for the DLR_{trend} estimated from the CRU data

long-term trends (Paltridge et al. 2009; Thorne and Vose 2010; Dessler and Davis 2010), both HadCRUH and ERA show consistently increasing q over land from the mid-1970s, rising to a sharp peak that coincides with the strong 1997/8 El Nino event, and remaining stable or decreasing slightly thereafter (Fig. 4a in Simmons et al. 2010). Nevertheless, the q anomalies since 1998 are still much higher than those in earlier years prior 1998 and there is an evident long-term increasing trend in surface q.

In response to the surface and atmosphere increases in q, ERA DLR_{trend} is overwhelmingly positive and the increase is generally strongest over driest regions (Fig. 9c). Note that the spatial coupling between DLR_{trend} and T_{trend} is weaker in ERA than in OBS because ERA DLR is estimated from an instantaneous forecast field accumulated from the start time step of the forecast everyday rather continuously from the start day of our study period. For example, there are also few regions (e.g., the western US) with decreasing q and DLR_{trend}, possibly due to data uncertainties in the ERA as they are inconsistent with the observed warming patterns and the ALL simulations (Figs. 1, 5, 10). Again, there is a negative logarithmic DLR_{trend}–EVI relationship (Fig. 9d, e), with R^2 = 95 and 79 % for the case of 7 and 35 ecoregions, respectively. The corresponding R^2 values for the linear fit are 81 and 65 %. Similar results also exist for other classifications (Table 4).

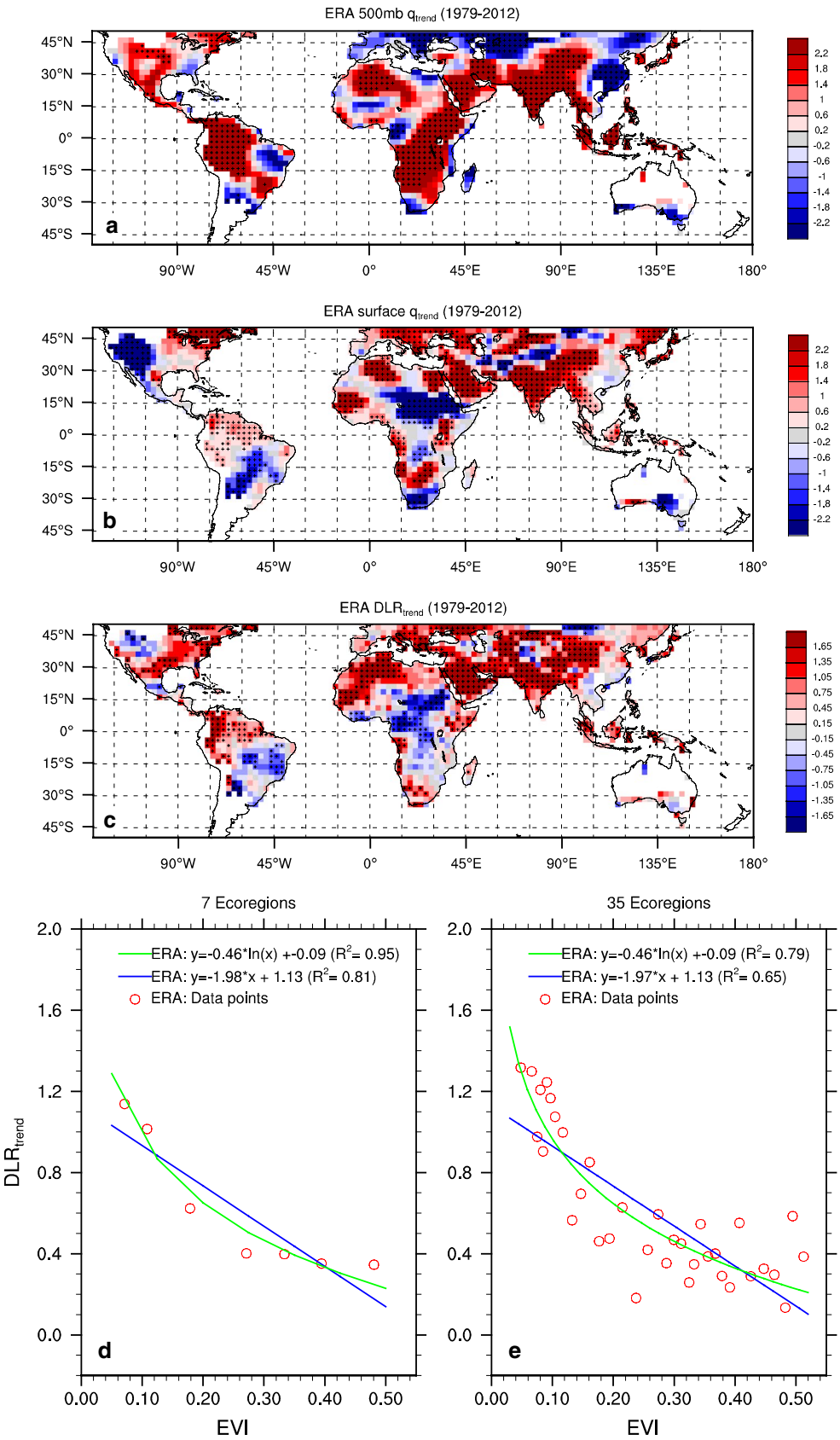

Fig. 9 Spatial patterns of ERA **a** 500 mb q_{trend} (%/10 years), **b** surface q_{trend} (%/10 years), and **c** DLR_{trend} (W/m^2/10 years) in the months of March–November (M–N) for the period 1979–2012. *Stippling* indicates regions where the trend is statistically significant ($p < 0.05$). **d**, **e** Same as Fig. 8c, d but for the ERA DLR_{trend}. q_{trend} (g/kg/10 years) is divided by the climatology q (g/kg) over the period 1979–2012 to represent the percent change in q (%/10 years)

Is it possible that the increasing q and DLR shown above may reflect primarily a circular effect between near surface AWV and surface warming (e.g., stronger surface warming may drive stronger DLR)? To gain more insight into this, we analyze the changes in surface q and DLR from the CMIP5 simulations. At the grid level, q_{trend} and DLR_{trend} in ALL (Fig. 10a, b) resembles each other in the spatial patterns, with a spatial correlation of 0.61 ($p < 0.001$), and show dominantly increasing trends. Among the 1338 land grids, 99.9 % exhibit a statistically significant positive trend ($p < 0.05$) for both q and DLR. The largest increases in q and DLR over the driest regions such as the Sahara desert and the Arabian Peninsula are expected to have the strongest impact on T as discussed previously. In contrast, only few regions show an increasing trend in surface q and DLR in NAT (Fig. 11), suggesting that anthropogenic forcings is the primary cause for the increases in q and DLR in ALL. Furthermore, among the 1338 land grids, only 13 and 15 % exhibit a statistically significant positive trend ($p < 0.05$) for q and DLR, respectively. At the ecoregion level, there is a negative logarithmic DLR_{trend}–EVI relationship (Fig. 9c, d) in ALL, with $R^2 = 87$ and 77 % for the case of 7 and 35 ecoregions, respectively. The corresponding R^2 values for the linear fit are 68 and 60 %. Such results also apply to other classifications (Table 5). On the contrary, the DLR_{trend}–EVI relationship in NAT differs substantially from that in ALL. These results, together with those from CRU and ERA, support our proposed hypothesis that the largest increases of DLR associated with increasing AWV may be the main radiative driver for the observed strongest warming over the driest ecoregions.

Histograms of T_{trend} for ALL and NAT, together with those from OBS and ERA, are shown in Fig. 12a. In general, ERA and ALL show distributions similar to OBS, but ERA has a wider range of T_{trend} and more extreme values, indicating stronger spatial variability than OBS, while ALL is within the observed T_{trend} range and has a narrower distribution skewed to the right (warming) side, indicating higher warming rates and stronger spatial coherence in ALL than OBS. In contrast, the multi-model ensemble mean in NAT and the 14 individual simulations show small and equal possibilities of cooling and warming trends, which are mostly skewed to the left side (cooling and small warming) and outside the range of ALL and OBS, indicating again that the role of anthropogenic forcing in reproducing the observed warming patterns. The corresponding histograms of DLR_{trend} are shown in Fig. 12b. As expected, DLR_{trend} has distributions similar to T_{trend}. The only exception is that unlike OBS and ALL, ERA is skewed to the left side, showing equal chances of positive and negative trends. Possibly ERA DLR_{trend} may have systematic biases because DLR is estimated from an instantaneous forecast field as mentioned previously. Again, NAT simulations have a distribution of DLR_{trend} that is mostly far outside the range of ALL, indicating again that the role of human influence in reproducing the observed DLR_{trend} patterns.

3.3.2 *Ecosystem feedbacks*

The magnitude of T_{trend} also depends on ecosystem feedbacks in response to surface radiative forcing. For wetter ecoregions, the surface warms less because more energy is converted into latent heat via ET and less energy for the increase of T. As EVI largely reflects the geographical distribution of amount of vegetation and SM, one may intuitively attribute the ecoregion-dependent warming to ecosystem feedbacks.

The classical hydrological framework characterizes ET as a function of SM into three climate regimes: wet (energy-limited) and dry (SM-limited) regimes, where SM does not impact ET variability, and a transitional regime, where SM strongly constrains ET variability and thus has a potential positive SM-T feedback (Seneviratne et al. 2006, 2010). In other words, climate changes naturally without anthropogenic forcing, and the transitional zones may warm faster than other climatic zones as they amplify the warming simply as a result of the positive SM-T feedback. This helps to explain the large warming trends in several transitional zones simulated in NAT (Fig. 6). However, the strongest warming rates are observed over the driest ecoregions, not in the transitional zones, indicating that SM and vegetation in deserts are too limited to have a strong feedback. Aridity and scarcity of vegetation in moisture-deprived regions are likely a consequence of the limited availability of moisture, rather than the cause of desert amplification.

Nevertheless, we cannot exclude the possibility that ecosystem feedbacks may still play a role in forming the observed warming patterns because land surface schemes used in ERA and CMIP5 are capable to intrinsically describe the classic framework of ET dependence on SM in representing land surface processes (Seneviratne et al. 2010). Furthermore, OBS does exhibit stronger warming in the transitional zones than wetter climatic zones. It should be also mentioned that the negative logarithmic DLR_{trend}–EVI relationship remains robust across all seasons (figures not shown for brevity), but the negative logarithmic T_{trend}–EVI relationship is absent in DJF (Table 3). This might indicate that ecosystem feedbacks are needed in forming the relationship as land–atmosphere coupling is stronger in warm seasons (e.g., Guo and Dirmeyer 2013; Dirmeyer et al. 2013) in the Northern Hemisphere where most of arid and semi-arid regions are located. In particular, DJF is the season when vegetation growth minimizes (and so does ET) and snow cover maximizes (and so does the snow-albedo feedback).

It is interesting to note that ERA shows positive biases in several transitional climate zones identified as hot spots for

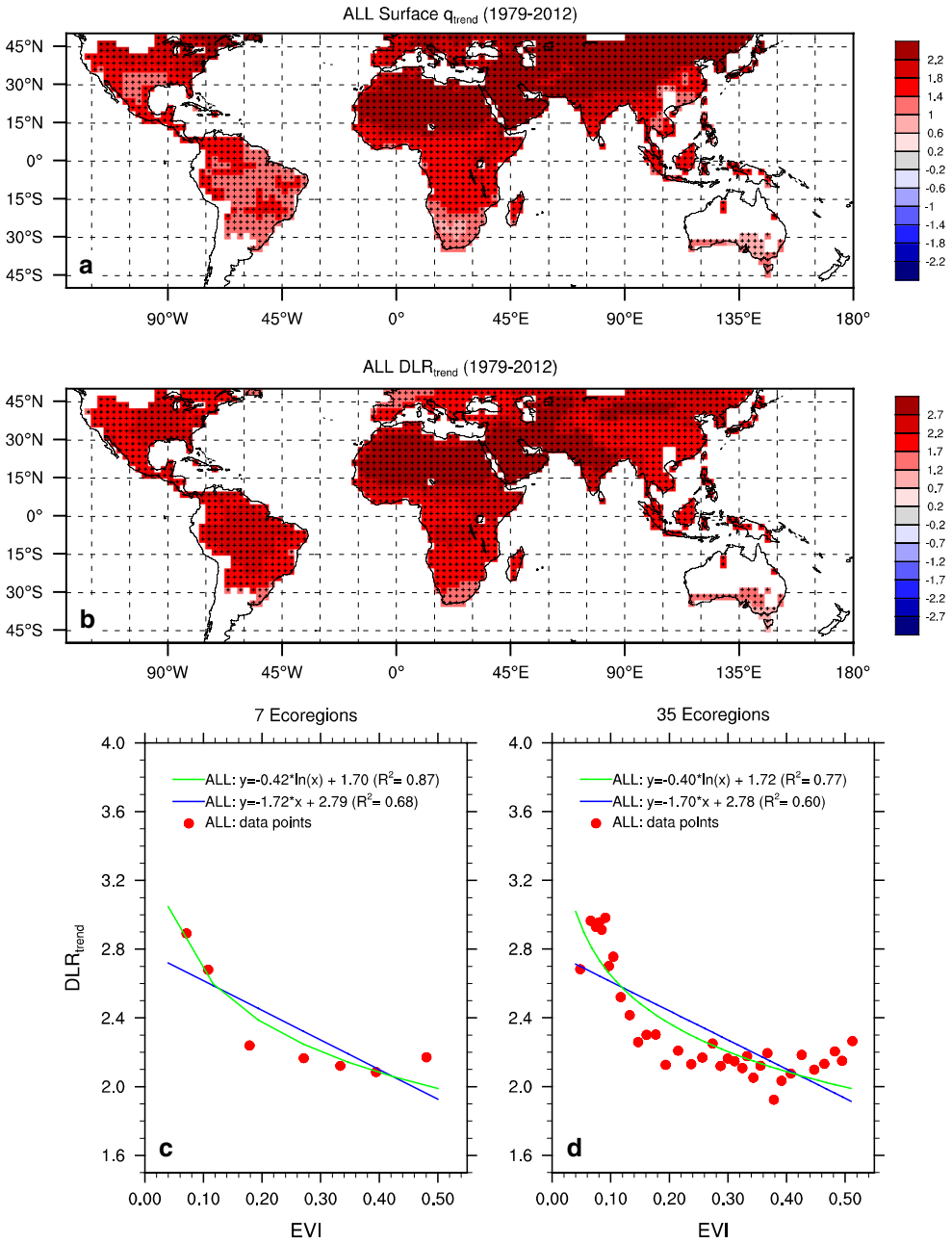

Fig. 10 **a–d** Same as Fig. 9b–e but for the CMIP5 multi-model ensemble mean surface q_{trend} and DLR_{trend} in ALL

strong land–atmosphere coupling in previous studies (e.g., Koster et al. 2004; Seneviratne et al. 2006, 2010; Guo and Dirmeyer 2013), particularly over the central Great Plains of North America, central and eastern Sahel, northern equatorial Africa, Eastern Asia and southern Europe (Fig. 4b). These large positive biases indicate that ERA may have overestimated the SM-T feedback over these zones. Negative ERA biases are seen over most regions in North and South Africa, and South Asia, particularly over the driest regions such as the Sahara desert (Fig. 4b), possibly linked to the positive cloud cover biases (figure not shown for brevity).

3.3.3 Other factors

Surface T can be also modified by variations in DSR due to changes in atmospheric conditions such as aerosols, cloud cover and precipitation (e.g., Wild et al. 2007; Wang and Dickinson 2013a, b). Large variability and uncertainties of these variables in observations, reanalysis data and climate simulations make it difficult to quantify their individual role in explaining the observed T_{trend}–EVI relationship. For example, except few areas with consistent trends, TCC_{trend} from CRU, ERA, and ALL differs not only in the

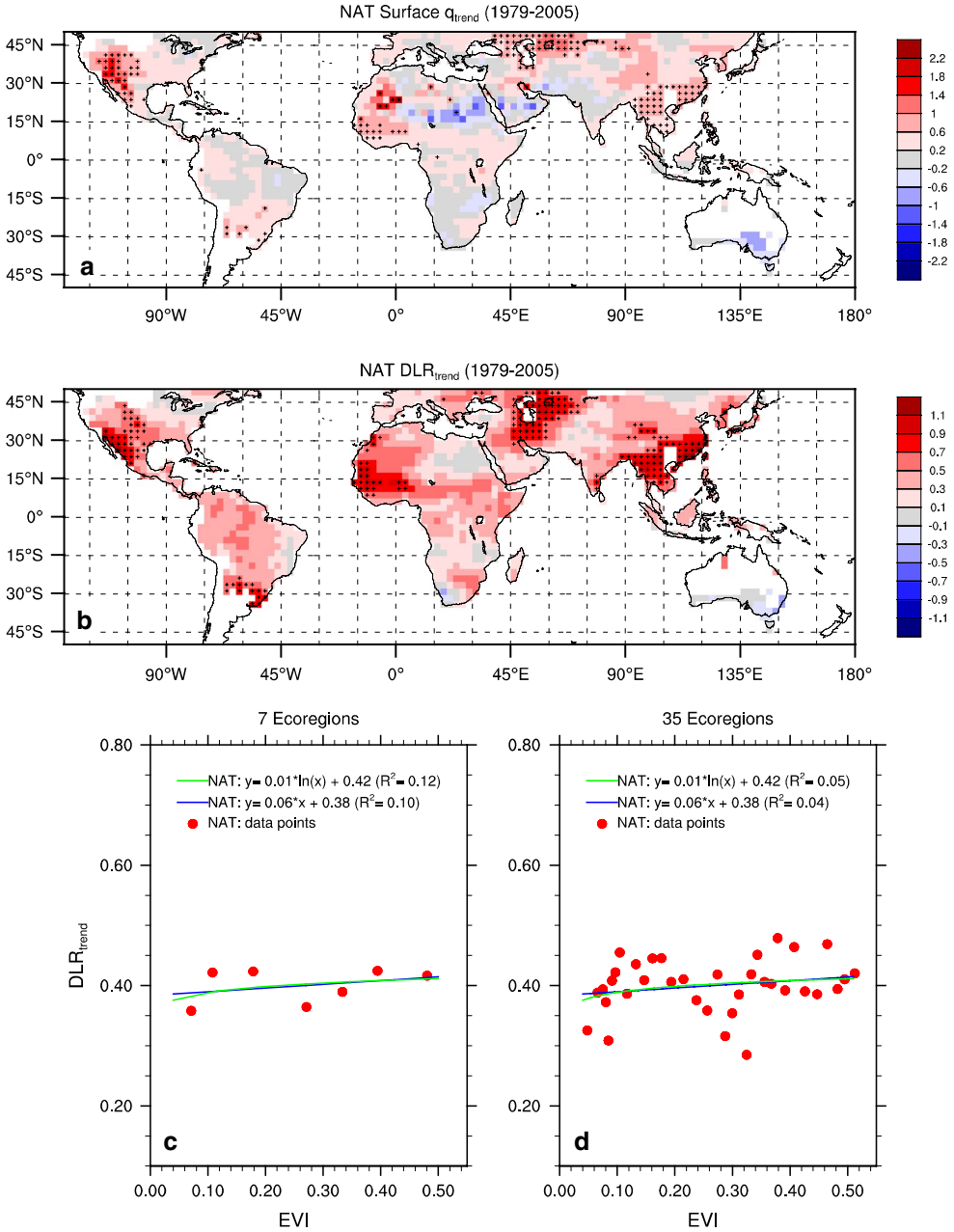

Fig. 11 Same as Fig. 10 but for the CMIP5 multi-model ensemble mean in NAT

sign, but also in the geographical distributions over many regions (figures not shown for brevity). Changes in TCC are expected to affect the trends of DLR and DSR and consequently the T_{trend}–EVI relationship. Such differences, on the one hand, indicate large TCC uncertainties among these datasets. On the other hand, despite such differences, the consistent negative logarithmic relationship (T_{trend}–EVI and DLR_{trend}–EVI) among OBS, ERA and ALL suggests that the positive water vapor feedback may represent the first-order mechanism driving the strongest warming over the driest ecoregions, where the impact of TCC is mostly limited.

To quantify whether the T_{trend}–EVI relationship is related to changes in TCC, DSR, and precipitation, we perform similar analyses as done above but replace T by each of these three variables. However, we cannot identify a meaningful relationship with the warming rates. Very likely changes in aerosols, clouds and precipitation often have considerable spatiotemporal variability and thus may have no strong spatial dependence of long-term trends on EVI when averaged at large scales, while the steady global-scale GHGs forcing may eventually primarily determine the large-scale T_{trend} patterns (Zhou et al. 2007, 2009). For example, Wang and Dickinson (2013b) found that at global

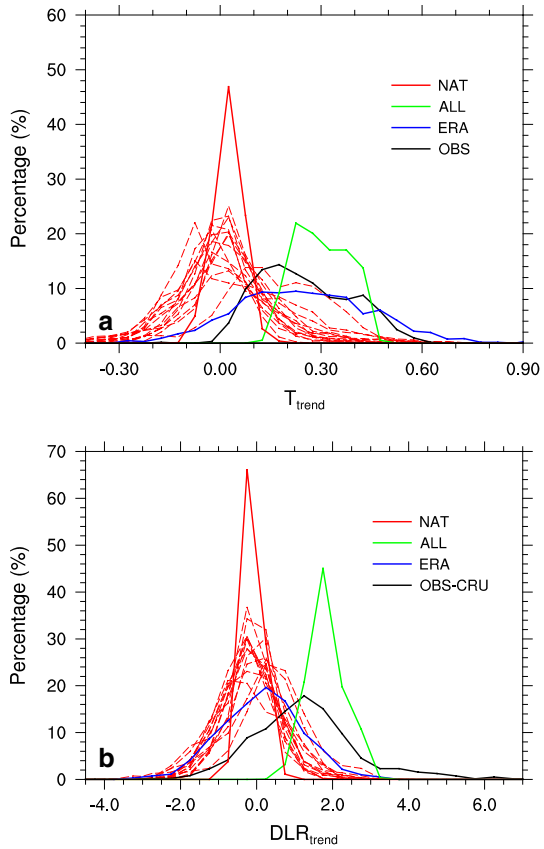

Fig. 12 Histogram of **a** T_{trend} (°C/10 years) and **b** DLR_{trend} (W/m^2/10 years) in the months of March–November (M–N) at the grid level from OBS, ERA, ALL and NAT for the period 1979–2012. The histograms for the 14 individual simulations in NAT (*dashed red lines*) are also shown. The DLR_{trend} estimated from the CRU data (OBS-CRU) is used to represent OBS in (**b**)

scales DSR over land changed little after the 1970s and had no apparent correlations with the changes in T. Similarly, short-term T variations are often associated with El Nino/southern oscillation, volcanic aerosols and solar variability, but these factors have small and limited effects on the long-term warming trends, particularly after 1979 (Foster and Rahmstorf 2011).

We also perform similar analyses to all other variables related to surface radiative and non-radiative fluxes in ERA and CMIP5 but cannot identify a meaningful association with the warming rates either. The only exception is upward longwave radiation (ULR), which shows features similar to DLR at both the grid and ecoregion levels, in response to the warming of T_{trend}. This is expected as ULR is strongly controlled by surface temperature and the amount of clouds and water vapor in the atmosphere, particularly near the surface. Drier ecosystems with less cloudiness and AWV lose more energy to out space via thermal emission because of smaller greenhouse effects of the near-surface atmosphere.

Deserts are very dry and mostly cloud-free due to the subsiding air that rises over the tropics. Their air can be warmed efficiently by the powerful greenhouse effect of increasing AWV as discussed previously, not by the release of latent heat because the descending air inhibits condensation. This heating effect is radiative in nature and manifested as enhanced DLR. We attribute the observed desert amplification primarily to the positive water vapor feedback because T_{trend} and DLR_{trend}, which is tightly linked to the increasing trend in AWV, show the best spatial correlations from the grid level to ecoregions than any other variables examined. This is not surprising, since warming and increased specific humidity are two of the most robust responses of the lower troposphere to increasing GHGs (Dirmeyer et al. 2013).

We realize that other climate feedbacks may also play a role in desert amplification. One good example is possible influence of the broadening and intensified subsidence linked to the poleward expansion of the Hadley cell under global warming (e.g., Lu et al. 2007), which could warm the lower troposphere adiabatically and increase DLR. Such changes in subsidence can be caused by enhanced GHGs (e.g., Fu 2015), and/or natural decadal SST variability (e.g., Quan et al. 2014). Similarly, the absence of T_{trend}–EVI relationship in DJF might be associated with inter-hemispheric asymmetry in the seasonality of baroclinicity and seasonal changes in the Hadley cell structure (Mitas and Clement 2006). In addition, Planck feedback and lapse-rare feedback (Pithan and Mauritsen 2014) could also have an impact because the atmospheric thermodynamic structure may be changed as well.

There are also some limitations in our attribution. The GHGs-induced changes in radiative forcing, combined with compounding changes in both hydrological and ABL processes, make it very difficult to untangle complex interactions in the context of a fully coupled land–atmosphere system, to reach consensus at the global scale. ERA data and CMIP5 simulations have biases as discussed previously. In particular, climate models tend to overestimate the warming of T in warm, dry climates linked with the surface moisture budget (Christensen and Boberg 2012) and to underestimate the T response to forcing under conditions of stable-stratification (Davy and Esau 2014) that represents the desert ABL at nighttime. Therefore, further research is needed to provide a comprehensive and complete picture of warming amplification over dry ecoregions.

4 Conclusions

Zhou et al. (2015) found that the warming rate observed for the period 1979–2012 increases dramatically with decreasing vegetation greenness over land between 50°S

and 50°N, with the strongest warming rate seen over the driest regions such as the Sahara desert and the Arabian Peninsula, suggesting warming amplification over deserts. To further this finding, we explore possible mechanisms for this warming amplification by analyzing observations, reanalysis data and historical simulations of AOGCMs from the CMIP5 archives. We examine various variables, related to surface radiative forcing, land surface properties, and surface energy and radiation budget, that control the warming patterns in terms of large-scale ecoregions. Our results indicate that desert amplification is likely attributable to enhanced longwave radiative forcing associated with a stronger water vapor feedback over drier ecoregions in response to the positive global-scale greenhouse gas (GHG) forcing. This warming amplification and associated downward longwave radiation at the surface are reproduced by historical simulations of AOGCMs with anthropogenic and natural forcings, but are absent if only natural forcings are considered, pointing to new potential fingerprints of anthropogenic warming.

These results, together with Zhou et al. (2015), suggest a fundamental pattern of global warming over land that depend on the dryness of ecosystems in mid- and low-latitudes. This ecoregion-dependent warming may reflect mostly the first order large-scale thermodynamic component of global warming linked to changes in the water and energy cycles over different ecoregions (Zhou et al. 2015). Ecosystem feedbacks may play a minor role in desert amplification as soil moisture and vegetation in deserts are too limited to have a strong feedback. Aridity and scarcity of vegetation in moisture-deprived regions are likely a consequence of the limited availability of moisture, rather than the cause of desert amplification.

This finding has important implications in interpreting global warming patterns and assessing climate change impacts. Climate models project drying over many areas in low- and mid-latitudes under increasing GHG concentrations (Trenberth et al. 2013). In particular, there is a strong tendency for the wet areas to get wetter and dry areas to get drier (Seager et al. 2010). Consequently, desert amplification may accelerate over the dry areas in the context of a warming climate and thus have important societal and economic consequences. Given uncertainties in ERA data and CMIP5 simulations, further research with more observational and modeling studies is needed to provide a full picture of mechanisms for desert amplification.

Acknowledgments This study was supported by National Science Foundation (NSF AGS-1247137 and AGS-1535426). H.C. was funded by National Natural Science Foundation of China (Grant Number 41230422). N.W. was supported by the China Scholarship Council (CSC) and by the University at Albany, State University of New York.

References

Christensen JH, Boberg F (2012) Temperature dependent climate projection deficiencies in CMIP5 models. Geophys Res Lett 39:L24705. doi:10.1029/2012GL053650

Dai A (2006) Recent climatology, variability and trends in global surface humidity. J Clim 19:3589–3606

Dai A (2013) Increasing drought under global warming in observations and models. Nat Clim Change 3:52–58. doi:10.1038/NCLIMATE1633

Davy R, Esau I (2014) Global climate models' bias in surface temperature trends and variability. Environ Res Lett 9(11):114024

Dee DP, Uppala SM, Simmons AJ, Berrisford P, Poli P, Kobayashi S, Andrae U, Balmaseda MA, Balsamo G, Bauer P, Bechtold P, Beljaars ACM, van de Berg L, Bidlot J, Bormann N, Delsol C, Dragani R, Fuentes M, Geer AJ, Haimberger L, Healy SB, Hersbach H, Hólm EV, Isaksen L, Kållberg P, Köhler M, Matricardi M, McNally AP, Monge-Sanz BM, Morcrette J-J, Park B-K, Peubey C, de Rosnay P, Tavolato C, Thépaut J-N, Vitart F (2011) The ERA-Interim reanalysis: configuration and performance of the data assimilation system. Q J R Meteorol Soc 137:553–597. doi:10.1002/qj.828

Deser C, Walsh JE, Timlin MS (2000) Arctic sea ice variability in the context of recent atmospheric circulation trends. J Clim 13(3):617–633

Dessler AE, Zhang Z, Yang P (2008) Water-vapor climate feedback inferred fromclimate fluctuations. Geophys Res Lett 35:L20704. doi:10.1029/2008GL035333

Dessler AE, SM Davis (2010) Trends in tropospheric humidity from reanalysis systems. J Geophys Res 115:D19127. doi:10.1029/2010JD014192

Dirmeyer PA, Jin Y, Singh B, Yan X (2013) Trends in land-atmosphere interactions from CMIP5 simulations. J. Hydrometeorol. doi:10.1175/JHM-D-12-0107.1

ECMWF (2013) IFS documentation—Cy40r1, operational implementation 22 November 2013, Part IV: physical processes. http://old.ecmwf.int/research/ifsdocs/CY40r1/

Foster G, Rahmstorf S (2011) Global temperature evolution 1979–2010. Environ Res Lett 6:044022. doi:10.1088/1748-9326/6/4/044022

Fu R (2015) Global warming-accelerated drying in the tropics. Proc Natl Acad Sci USA 112(12):3593–3594. doi:10.1073/pnas.1503231112

Guo ZC, Dirmeyer PA (2013) Interannual variability of land–atmosphere coupling strength. J. Hydrometeorol 14:1636–1646. doi:10.1175/JHM-D-12-0171.1

Hansen J, Ruedy R, Sato M, Lo K (2010) Global surface temperature change. Rev Geophys 48:RG4004. doi:10.1029/2010RG000345

Harris I, Jones PD (2014) CRU TS3.22: Climatic Research Unit (CRU) Time-Series (TS) Version 3.22 of high resolution gridded data of month-by-month variation in climate (Jan. 1901–Dec. 2013). NCAS British Atmospheric Data Centre, 24 September 2014. doi:10.5285/18BE23F8-D252-482D-8AF9-5D6A2D40990C

Held IM, Soden BJ (2000) Water vapor feedback and global warming. Annu Rev Energy Environ 25:441–475

Huete A, Didan K, Miura T, Rodriguez EP, Gao X, Ferreira LG (2002) Overview of the radiometric and biophysical performance of the MODIS vegetation indices. Remote Sens Environ 83:195–213

IPCC (2007) Climate change 2007: the physical science basis, contribution of Working Group I to the Fourth Assessment Report of the IPCC. Cambridge University Press, Cambridge. ISBN:978 0521 88009-1

IPCC (2013) Climate change 2013: the physical science basis, the contribution of Working Group I to the Fifth Assessment Report of the Intergovernmental Panel on Climate Change. Cambridge University Press, Cambridge. ISBN:978-1-107-05799-1

Jeong SJ, Ho CH, Jeong JH (2009) Increase in vegetation greenness and decrease in springtime warming over east Asia. Geophy Res Lett 36:L02710

Jiménez-Muñoz JC, Sobrino JA, Mattar C, Malhi Y (2013) Spatial and temporal patterns of the recent warming of the Amazon forest. J Geophys Res Atmos. doi:10.1002/jgrd.50456

Koster RD et al (2004) Regions of strong coupling between soil moisture and precipitation. Science 305:1138–1140

Lu J, Cai M (2010) Quantifying contributions to polar warming amplification in an idealized coupled general circulation model. Clim Dyn 34:669–687

Lu J, Vecchi GA, Reichler T (2007) Expansion of the Hadley cell under global warming. Geophys Res Lett 34:L06805. doi:10.1029/2006GL028443

Malhi Y, Wright J (2004) Spatial patterns and recent trends in the climate of tropical rainforest regions. Philos Trans R Soc Lond B 359:311–329

McNider RT, Steeneveld GJ, Holtslag AAM, Pielke RA Sr, Mackaro S, Pour-Biazar A, Walters J, Nair U, Christy J (2012) Response and sensitivity of the nocturnal boundary layer over land to added longwave radiative forcing. J Geophys Res 117:D14106

Mitas CM, Clement A (2006) Recent behavior of the Hadley cell and tropical thermodynamics in climate models and reanalyses. Geophys Res Lett 33:L01810. doi:10.1029/2005GL024406

Myhre G, Highwood EJ, Shine KP, Stordal F (1998) New estimates of radiative forcing due to well-mixed greenhouse gases. Geophys Res Lett 25:2715–2718

Nagler PL, Scott RL, Westenburg C, Cleverly JR, Glenn EP, Huete AR (2005) Evapotranspiration on western US rivers estimated using the enhanced vegetation indices from MODIS and data from eddy covariance and Bowen ratio flux towers. Remote Sens Environ 97(3):337–351

Naud CM, Chen Y-H, Rangwala I, Miller JR (2013) Sensitivity of downward longwave surface radiation to moisture and cloud changes in a high elevation region. J Geophys Res 118(17):10072–10081. doi:10.1002/jgrd.50644

Paltridge G, Arking A, Pook M (2009) Trends in middle- and upper-level tropospheric humidity from NCEP reanalysis data. Theor Appl Climatol 98:351–359. doi:10.1007/s00704-009-0117-x

Philipona R, Durr B, Ohmura A, Ruckstuhl C (2005) Anthropogenic greenhouse forcing and strong water vapor feedback increase temperature in Europe. Geophys Res Lett 32:L19809. doi:10.1029/2005GL023624

Pithan F, Mauritsen T (2014) Arctic amplification dominated by temperature feedbacks in contemporary climate models. Nat Geosci 7:181–184. doi:10.1038/ngeo2071

Qu X, Hall A (2007) What controls the strength of snow-albedo feedback? J Clim 20:3971–3981. doi:10.1175/JCLI4186.1

Quan X-W, Hoerling M, Perlwitz J, Diaz H, Xu T (2014) How fast are the tropics expanding? J. Clim 27:1999–2013. doi:10.1175/JCLI-D-13-00287.1

Rangwala I, Sinsky E, Miller RJ (2013) Amplified warming projections for high altitude regions of the northern hemisphere mid-latitudes from CMIP5 models. Environ Res Lett 8:024040. doi:10.1088/1748-9326/8/2/024040

Ruckstuhl C, Philipona R, Morland J, Ohmura A (2007) Observed relationship between surface specific humidity, integrated water vapor, and longwave downward radiation at different altitudes. J Geophys Res 112:L19809. doi:10.1029/2005GL023624

Schneider T, O'Gorman PA, Levine XJ (2010) Water vapor and the dynamics of climate changes. Rev Geophys 48:RG3001. doi:10.1029/2009RG000302

Seager R, Naik N, Vecchi GA (2010) Thermodynamic and dynamic mechanisms for large-scale changes in the hydrological cycle in response to global warming. J Clim 23:4651–4668

Seneviratne SI, Lüthi D, Litschi M, Schär C (2006) Land–atmosphere coupling and climate change in Europe. Nature 443:205–209

Seneviratne SI, Corti T, Davin EL, Hirschi M, Jaeger EB, Lehner I, Orlowsky B, Teuling AJ (2010) Investigating soil moisture-climate interactions in a changing climate: a review. Earth Sci Rev 99(3–4):125–161

Simmons AJ, Willett KM, Jones PD, Thorne PW, Dee DP (2010) Low-frequency variations in surface atmospheric humidity, temperature, and precipitation: inferences from reanalyses and monthly gridded observational data sets. J Geophys Res 115(D1):D01110. doi:10.1029/2009JD012442

Sutton RT, Dong B, Gregory JM (2007) Land/sea warming ratio in response to climate change: IPCC AR4 model results and comparison with observations. Geophys Res Lett 34(2):L02701

Suzuki R, Masuda K (2004) Interannual co-variability found in evapotranspiration and satellite-derived vegetation indices over northern Asia. J Meteorol Soc Jpn 82(4):1233–1241

Taylor KE, Stouffer RJ, Meehl GA (2012) An overview of CMIP5 and the experiment design. Bull Am Meteorol Soc 93:485–498

Thorne PW, Vose RS (2010) Reanalyses suitable for characterizing long-term trends: are they really achievable? Bull Am Meteorol Soc 91:353–361

Thorne PW, Lanzante JR, Peterson TC, Seidel DJ, Shine KP (2010) Tropospheric temperature trends: history of an ongoing controversy. Clim Change, Wiley Interdisciplinary Reviews. doi:10.1002/wcc.80

Trenberth KE, Dai A, van der Schrier G, Jones PD, Barichivich J, Briffa KR, Sheffield J (2013) Global warming and changes in drought. Nat Clim Change 4:17–22

Vose RS et al (2012) NOAA's merged land–ocean surface temperature analysis. Bull Am Meteorol Soc 93:1677–1685. doi:10.1175/BAMS-D-11-00241.1

Wang KC, Dickinson RE (2012) A review of global terrestrial evapotranspiration: observation, modeling, climatology, and climatic variability. Rev Geophys 50(2):RG2005

Wang K, Dickinson RE (2013a) Global atmospheric downward longwave radiation at the surface from ground-based observations, satellite retrievals, and reanalyses. Rev Geophys 51:150–185. doi:10.1002/rog.20009

Wang KC, Dickinson RE (2013) Contribution of solar radiation to decadal temperature variability over land. Proc Natl Acad Sci 110(37):14877–14882. www.pnas.org/cgi/doi/10.1073/pnas.1311433110

Wang KC, Liang S (2009) Global atmospheric downward longwave radiation over land surface under all-sky conditions from 1973 to 2008. J Geophys Res 114:D19101. doi:10.1029/2009JD011800

Wild M, Ohmura A, Makowski K (2007) Impact of global dimming and brightening on global warming. Geophys Res Lett 34:L04702. doi:10.1029/2006GL028031

Willett KW, Jones PD, Gillett NP, Thorne PW (2008) Recent changes in surface humidity: development of the HadCRUH dataset. J Clim 21(5364):5383

Wunsch W (2005) The total meridional heat flux and its oceanic and atmospheric partition. J Clim 18:4374–4380. doi:10.1175/JCLI3539.1

Zhou L, Dickinson RE, Tian Y, Vose RS (2007) Impact of vegetation removal and soil aridation on diurnal temperature range in a semiarid region—application to the Sahel. Proc Natl Acad Sci USA 104(46):17937–17942

Zhou L, Dai A, Dai Y, Vose RS, Zou C-Z, Tian Y, Chen H (2009) Spatial dependence of diurnal temperature range trends on precipitation from 1950 to 2004. Clim Dyn 32:429–440. doi:10.1007/s00382-008-0387-5

Zhou L, Dickinson RE, Dai A, Dirmeyer P (2010) Detection and attribution of anthropogenic forcing to diurnal temperature range changes from 1950 to 1999: comparing multi-model simulations with observations. Clim Dyn 35:1289–1307. doi:10.1007/s00382-009-0644-2

Zhou L, Chen H, Dai Y (2015) Stronger warming amplification over drier ecoregions observed since 1979. Environ Res Lett 10:064012. doi:10.1088/1748-9326/10/6/064012